

Flat band localization in twisted bilayer graphene nanoribbons

Elias Andrade,^{1,*} Pierre A. Pantaleón,² Francisco Guinea,^{2,3,4} and Gerardo G. Naumis^{5,†}

¹*Posgrado en ciencias Físicas, Instituto de Física, Universidad Nacional Autónoma de México (UNAM). Apdo. Postal 20-364, 01000 México D.F., México*

²*IMDEA Nanoscience, Faraday 9, 28049 Madrid, Spain*

³*Donostia International Physics Center, Paseo Manuel de Lardizábal 4, 20018 San Sebastián, Spain*

⁴*Ikerbasque, Basque Foundation for Science, 48009 Bilbao, Spain*

⁵*Depto. de Sistemas Complejos, Instituto de Física, Universidad Nacional Autónoma de México (UNAM). Apdo. Postal 20-364, 01000 México D.F., México*

(Dated: September 14, 2023)

We analyze the electronic structure of twisted bilayer graphene (TBG) nanoribbons close to the magic angle. We describe a transition from an incomplete to a complete moiré structure. By considering *zigzag* and *armchair* edge terminations, the low-energy bands are strongly modified, and thus, the edge flat band localization is sensitive to the type of boundary. By means of a scaled tight-binding model, we calculate the band structure and find that, for an *armchair* configuration, an incomplete moiré edge suppresses the edge localization, while for a *zigzag* configuration, we find a strong interference of the edge states with the moiré bands. In particular, for the *armchair* termination, we observe a competition between the ribbon periodicity and the graphene monolayers, which we describe with a potential well toy model. Furthermore, for ribbons with widths of multiple moiré cells, the flat bands of the moirés in the bulk are unperturbed as we change the borders. These results are explained in terms of the strong electronic localization, nearly Gaussian, in the AA stacking regions, as confirmed by an inverse participation ratio analysis. Our results demonstrate that the electronic structure of TBG nanoribbons is sensitive to the edge termination, offering an explanation for recent experimental results.

I. INTRODUCTION

Due to the interplay between non-trivial band topology and band flatness, magic angle twisted bilayer graphene (TBG) has shown to be an ideal platform for the appearance of a plethora of topological and correlated phases, including for example non-conventional superconductivity [1, 2], correlated insulators [3–5], ferromagnetism [6], and other many body effects [7–24]. For magic angles the flat bands near the Fermi energy appear due to the localization of the electronic wavefunction at the AA-stacking sites, this was predicted [25–27] and then experimentally confirmed [28–32]. The wavefunction geometry comes from the modulated interlayer coupling, which can be seen as an effective moiré potential well [33–38].

Studies of TBG with reduced translational symmetry, for example in flakes, have shown that a single moiré cell may be enough to localize the wavefunction in the AA spots [39], supporting a “moiré quantum well” picture. However, theoretical [40–43] and experimental [44, 45] studies have demonstrated that both bulk and “moiré edge states” appear in TBG with a nanoribbon geometry. In particular, it has been shown that in the presence of a *zigzag* termination there is a coexistence of edge and bulk moiré states near the Fermi energy [45], and that the edge states are found at the edges of AB sites [40, 41].

On the other hand, recent experiments have shown the

breakdown of moiré flat bands in TBG due to edge termination [46]. In the experiment, the electronic localization is found to be persistent even if translational symmetry is broken as long as the moiré supercell is complete. However, when the supercell is incomplete, there is a strong suppression of the electronic localization resulting in a vanishing of the density of states near the Fermi Energy.

A useful methodology to analyze the transition from a complete to an incomplete supercell is by introducing an interlayer sliding between graphene layers, where the displacement between layers is particularly relevant in terminated TBG due the change in the borders at both the scales of the moiré lattice and the graphene lattice. This type of displacement is known to produce a topological charge pumping in the perpendicular direction of the displacement, characterized by a topological invariant known as the sliding Chern number [47–50].

In spite of this, while the topological sliding properties provide a description of the number of moiré edge states, the mechanism behind the breakdown of the flat bands as the portion of the moiré cell is reduced at the edges, as well as its relationship with electronic localization, is not clear. To address these questions, in this work, we analyze the electronic properties of TBG nanoribbons with different unit cells, ranging from an incomplete to a complete moiré supercell. We consider two nanoribbon geometries: *zigzag* and *armchair* [51, 52]. For each configuration, we monitor the electronic localization and the group velocity of the bands near the Fermi energy, and we distinguish between the contributions originating from the moiré scales of those of the graphene lattice. We find that the electronic structure is strongly sensitive to

* eandrade@estudiantes.fisica.unam.mx

† naumis@fisica.unam.mx;

<http://www.fisica.unam.mx/personales/naumis/>

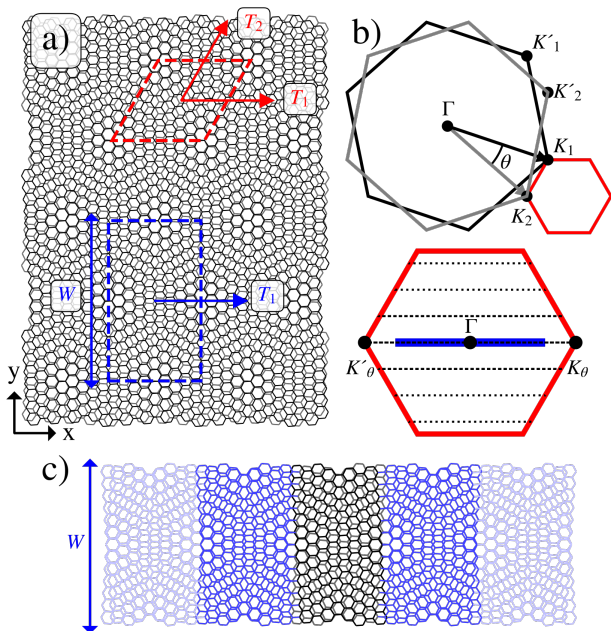


FIG. 1. a) Lattice structure of TBG with $\theta = 7.34^\circ$, red dashed line is the corresponding unit cell. The blue square cell is used to construct a nanoribbon of width W . b) Mini-Brillouin zone (red) resulting from the twist between layers. For the nanoribbon the Brillouin gets folded into the blue line as the momentum along the y -direction is quantized. c) Formation of the nanoribbon with the unit cell shown in a), here five unit cells are shown.

the edge configuration which may lead to the coexistence or suppression of edge and bulk moiré electronic localization. Our work demonstrates the significant dependence of the electronic structure of twisted bilayer graphene nanoribbons with the edge termination and may offer an explanation for the breakdown of the moiré flat bands found in Ref. [46].

The layout of this paper is as follows. In Sec. II, we present the model used composed of a minimum tight binding Hamiltonian [53] plus a rescaling approximation. In Sec. III we present our main numerical results concerning *armchair* terminated TBG nanoribbons, where we analyze the change on the electronic properties as a function of the completeness of the moiré supercell within the ribbon. In Sec. III C we discuss the change in energy of the bands as we increase the size of the moiré and explain them qualitatively through a toy-model. We also include a brief analysis regarding *zigzag* terminated TBG nanoribbons in Sec. IV. Finally in Sec. V we give our conclusions.

II. MODEL

We consider a TBG lattice as shown in Fig. 1a). The structure is defined by rotating the layer 1 and 2 of

the AA-stacked bilayer around the common center by $\pm\theta/2$, respectively. The lattice vectors of graphene are $a_1 = \sqrt{3}a(0, 1)$ and $a_2 = \sqrt{3}a(\frac{\sqrt{3}}{2}, \frac{1}{2})$, where $a \approx 1.42 \text{ \AA}$ is the distance between carbon atoms. Upon rotation, the lattice vectors on each layer are modified as $a_{1,2}^{u/d} = R(\pm\theta/2)a_{1,2}$. We consider a commensurate lattice [54, 55] such that the mismatch between layer produces a moiré pattern with lattice vectors given by

$$T_{1/2} = \frac{1}{2\sin(\theta/2)}R(-30^\circ)a_{1/2}. \quad (1)$$

We employ a minimum tight-binding Hamiltonian [53], which consists of an intralayer part H_{\parallel} and an interlayer part H_{\perp} , given by,

$$\begin{aligned} H &= H_{\parallel} + H_{\perp} \\ &= - \sum_{i \neq j, m} \gamma_{ij}^{m,m} (c_{m,i}^\dagger c_{m,j} + h.c.) \\ &\quad - \sum_{i,j,m} \gamma_{ij}^{m,m+1} (c_{m,i}^\dagger c_{m+1,j} + h.c.), \end{aligned} \quad (2)$$

where $c_{m,i}^\dagger$ and $c_{m,i}$ are creation and annihilation operators respectively, acting on site i and layer m , $\gamma_{ij}^{m,m}$ and $\gamma_{ij}^{m,m+1}$ are the intralayer and interlayer hopping integrals, respectively. For the intralayer hoppings only first-neighbors are considered, which have a constant value $\gamma_{ij}^{m,m} = t_{\parallel} = 3.09 \text{ eV}$. The interlayer hopping is considered to decay exponentially as,

$$\gamma_{ij}^{m,m+1} = t_{\perp} \frac{d_0^2}{r^2 + d_0^2} \exp\left(-\frac{\sqrt{r^2 + d_0^2} - d_0}{\lambda_{\perp}}\right), \quad (3)$$

where $t_{\perp} = 0.39 \text{ eV}$ is the hopping amplitude, $d_0 = 3.35 \text{ \AA}$ is the distance between layers and $\lambda_{\perp} = 0.27 \text{ \AA}$ is a modulation of the interlayer hopping.

To reduce the number of atoms and the computational cost in the numerical calculations, we employ a re-scaling approximation [56–58], where the bands in TBG depend only on a single dimensionless parameter α given by [59],

$$\alpha = \frac{\sqrt{3}at_{\perp}}{2\hbar v_f \sin(\theta/2)} \propto \frac{t_{\perp}}{t_{\parallel} \sin(\theta/2)}, \quad (4)$$

here t_{\perp} refers to an average of the interlayer hopping and v_f is the Fermi velocity. The importance of this relation is that the dependence on the ratio of the hopping integrals and angle allows us to explore the low-energy physics of a TBG system with a given α using a larger angle and thus reducing the number of atoms in the unit cell. To do this, we use re-scaled intralayer hopping integral,

$$t_{\parallel} \rightarrow \frac{t_{\parallel}}{\Lambda}, \quad (5a)$$

where,

$$\Lambda = \frac{\sin(\theta'/2)}{\sin(\theta/2)}. \quad (5b)$$

In the above equation, θ' is the angle used to simulate the spectrum of a system with angle θ . Furthermore, to preserve the length of the moiré-cell, a re-scaling of the distances must be done as well,

$$a \rightarrow \Lambda a. \quad (6)$$

This re-scaling approximation allow us to simulate the magic angle $\theta = 1.08^\circ$ which has a unit cell of about 11×10^3 atomic sites. In particular, with an angle $\theta' = 2.28^\circ$ which has 5048 atoms, the low energy band structure is nearly identical to that of the magic angle if we use a scaling factor of $\Lambda = 2.11$ in Eq. 5, thus making computational calculations more attainable.

III. ARMCHAIR TERMINATED TBG NANORIBBONS

A. Electronic Structure

By using the methodology described in the previous section, we first consider the case of *armchair* terminated TBG nanoribbons. This configuration is the same as that in Fig. 1c) where the periodicity is along the horizontal direction. In Fig. 2 we show the corresponding spectrum with a single moiré ≈ 11.3 nm considering different moiré terminations. In Fig. 2a) the AA regions at the moiré center coincide with the ribbon center and the moiré cell is mostly complete, thus the usual localization at the AA regions occurs and flat bands can be seen, in agreement with previous results in TBG flakes [39]. Meanwhile, in Fig. 2b) the moiré cells are split in halves with the AA regions at the edges. These half-moiré cells are not sufficient to localize the wavefunction at low-energies and the resulting spectrum is dispersive.

In Fig. 3 we further study this transition in ribbons of width $W = 22.6$ nm, around the length of two moirés, ensuring that there is always at least one complete moiré within the ribbon. We characterize different moiré terminations with a sliding parameter δ [47–50], such that it translates the ribbon cell within the TBG lattice, starting from $\delta = 0$, cf. Fig. 3g), where the moiré is centered with the ribbon, to $\delta = 0.25W$, cf. Fig. 3l), where the center of the ribbon is between two moirés. In Fig. 3a)-f) we show the energy spectrum around the Fermi energy (E_f) for six different configurations. For each band structure, we show in blue the four lowest energy bands and the next four in red. Note that the sliding structure is periodic in δ such that $\delta = 0.3W$ corresponds to Fig. 3e) with the unit cell upside down. In Figs. 3g)-l) and Figs. 3m)-r) we show the corresponding total charge density of the bands for each system.

In Fig. 3a) for $\delta = 0$, there are four narrow bands near E_f which correspond to states mainly localized at the AA regions within the whole moiré cells. There is also localization at the incomplete moirés, but it occurs at higher energies, as shown in Fig. 3m). Interestingly, by following the sequence of panels in Fig. 3, as we increase

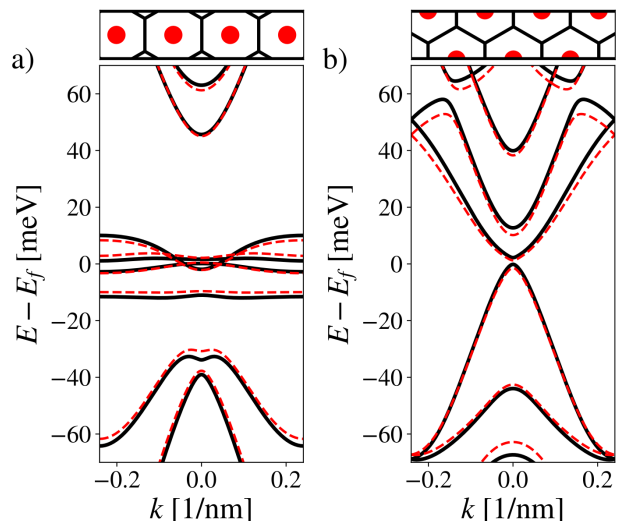


FIG. 2. Low energy band structure for a TBG nanoribbon of the width of one moiré cell with twist angle $\theta = 1.08^\circ$ (black solid line) and with $\theta' = 2.28^\circ$ using the rescaling to simulate θ (red dashed line). Above each band structure a schematic of the geometry of each ribbon is shown, where the red circles indicate the AA stacking regions. For a) the moiré is complete with the AA regions located at the center of the ribbon. As the moiré cell is complete, states get localized here and flat bands appear around the Fermi energy. In b) the moirés are split in halves with the AA regions at the edges, the spectrum around the Fermi energy is dispersive.

δ , the half moiré cell at the bottom starts to disappear while the upper one grows. Intuitively, the increase in the upper portion of the moiré allows the localization of the wavefunction in a greater area, lowering its energy towards E_f , and also reducing its group velocity. This effect is clearly seen in Figs. 3a)-d) where four red dispersive bands are flattened and pushed towards the center of the energy spectrum, thus increasing their localization in the AA centers, as shown in Figs. 3g)-r).

However, although there is an increase in the size of the incomplete moiré, the red band closer to E_f in Fig. 3d), is further away in Fig. 3e), which is also reflected in the absence of hybridization between states of the two moirés in Fig. 3k) and Fig. 3q). This indicates that the decreasing of the moiré bands energy towards E_f is non-monotonous. We further explore this behavior in Fig. 4, where we plot the spectrum at the boundary of the Brillouin zone as a function of δ . We observe an oscillatory behavior of the energy bands, which we found to be influenced by the sliding parameter in two distinct ways. Firstly, there is a general tendency of the remote bands to transition from being dispersive to becoming narrow and merge with the flat bands. This occurs near $\delta = 0.25W$. By continuing to increase the sliding parameter, it is equivalent to moving backward in the plot. This large-scale wavelength oscillation has been described

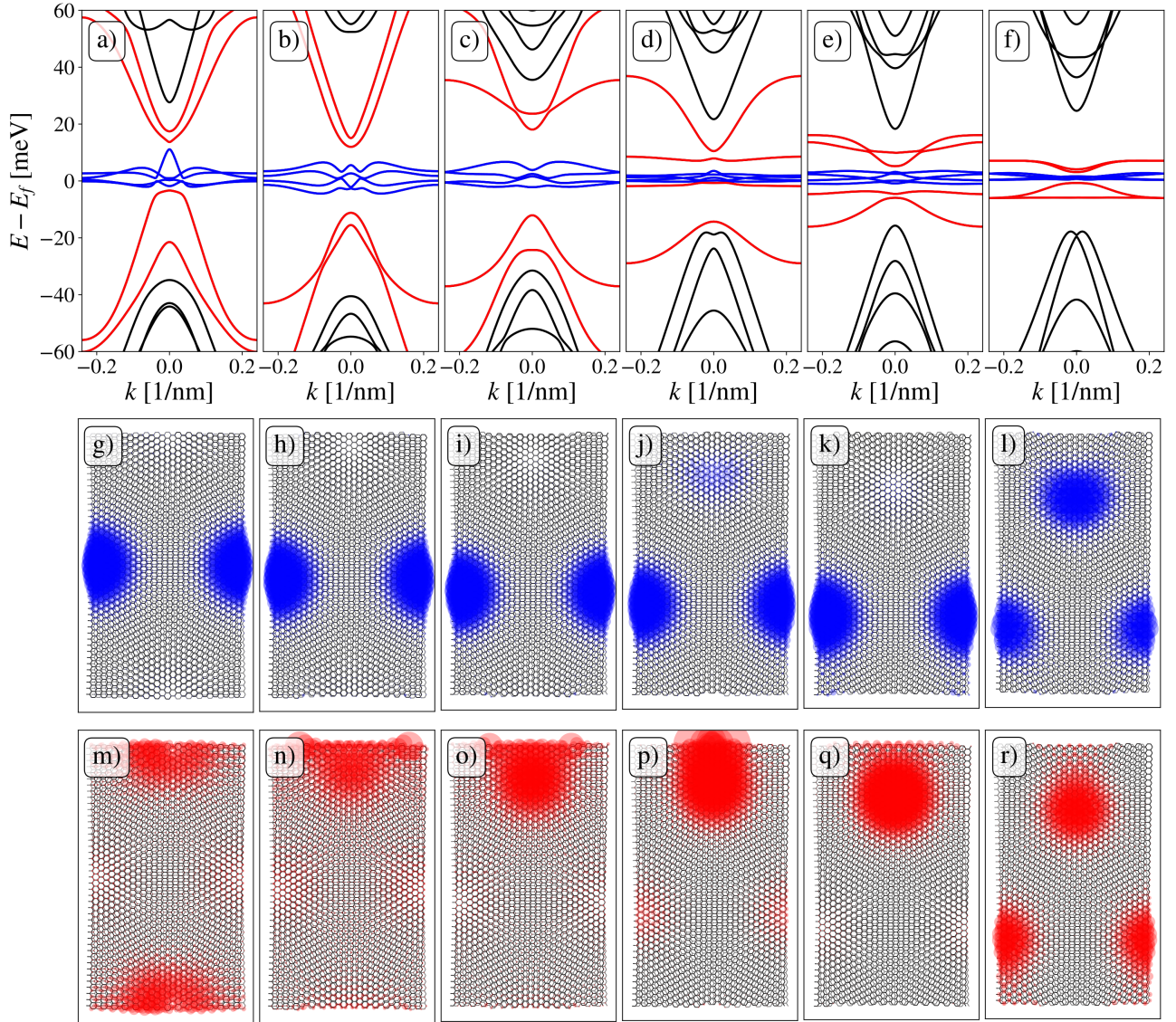


FIG. 3. Low energy band structure for *armchair* terminated TBG nanoribbons simulating a twist angle $\theta = 1.08^\circ$ with constant width $W = 22.6$ nm, we consider different moiré terminations by translating the unit cell of the ribbon by a) $\delta = 0$, b) $\delta = 0.05W$, c) $\delta = 0.1W$, d) $\delta = 0.15W$, e) $\delta = 0.2W$, f) $\delta = 0.25W$. The blue bands are the four lowest energy bands, these states are localized at the complete moiré. The next four energy bands are shown in red, these correspond to the incomplete moiré and as we change the termination, increasing the size of the incomplete moiré the bands get flatter and go towards E_f . In g)-l) we show the total charge density of the blue bands respectively to a)-f) within the unit cell, while in m)-r) for the red bands.

as a topological sliding effect in Refs. [47–50]. Secondly, the bands display a short wavelength oscillation not described before, which we attribute to an interference effect at the atomic scale, (cf. Sec. III C).

To analyze these oscillatory effects, in Fig. 4a), we show the bands for two different ribbon widths (black and blue lines), while Fig. 4b) displays the same bands without the scaling approximation. Thus, a comparison between both figures indicates that the long wavelength oscillations remain unchanged, but the short wavelength

oscillations are different. This suggests that the transition of the bands from being dispersive to becoming narrow is a moiré scale effect, is independent of the ribbon size, and is mainly controlled by the percentage of the incomplete moiré at the boundary. Furthermore, we notice that without the re-scaling of the atomic distances, the short wavelength oscillation in Fig. 4b) is invariant, and has a value of $\lambda = \sqrt{3}a/2$. This associate the oscillatory effect to the edges of the microscopic graphene lattice and cannot be effectively mapped with the re-scaling ap-

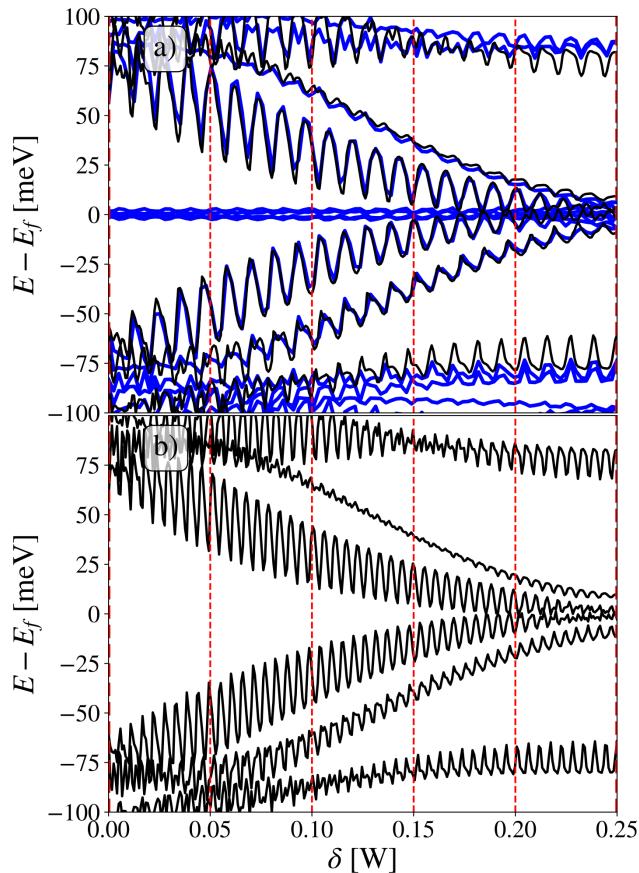


FIG. 4. Spectrum at the edge of the Brillouin zone as a function of δ . For a) the rescaling is used, we show in black the spectrum for a ribbon of the width of one moiré and in blue for a width of two moirés. It can be seen how the four bands go towards E_f as we increase δ , furthermore these bands lower their energy independently of the width of the ribbons, as these bands only depend on the moiré that is being formed at the border. The complete moirés in the bulk will just result in more flat bands around E_f . In b) for the width of one moiré without rescaling, the wavelength of the oscillation increases as these come from the microscopic borders which is not equal within the re-scaling, but the overall behavior is retained. The dashed red vertical lines indicate the values of δ used in Fig. 3.

proximation. Thus, in Fig. 4a), due to the re-scaling, the oscillation has a larger wavelength given by $\lambda' = \Lambda\lambda$ in comparison with Fig. 4b) without re-scaling. We further describe this effect in Sec. III C.

B. Charge localization

The effect of an incomplete moiré cell at the edge is depicted in Fig. 5a), where we show the density of states (DOS) near the E_f for the six borders considered in Fig. 3. As δ increases more states move to-

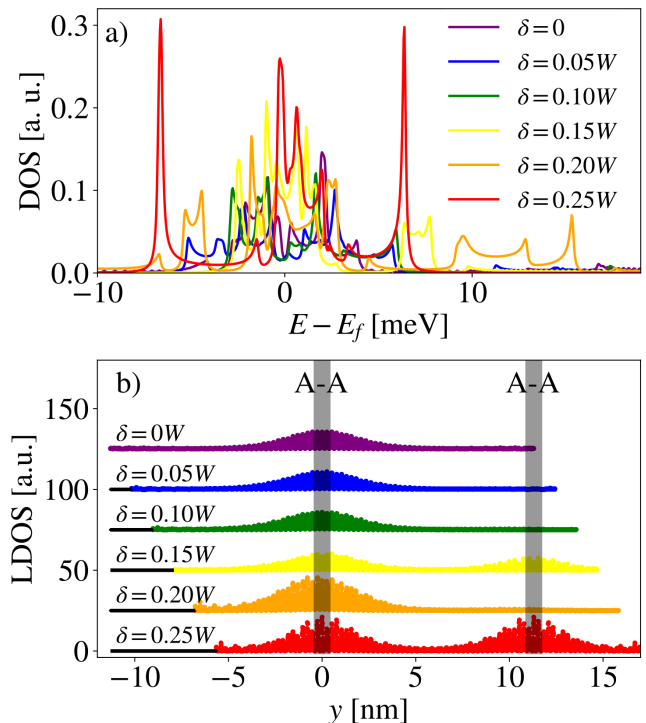


FIG. 5. a) Density of states near E_f for the ribbons shown in Fig. 3, denoted in different colors for $\delta = 0$ (purple), $\delta = 0.05W$ (blue), $\delta = 0.10W$ (green), $\delta = 0.15W$ (yellow), $\delta = 0.20W$ (orange) and $\delta = 0.25W$ (red). b) Local density of states (LDOS) of the four nearest bands to E_f (blue bands in Fig. 3 a)-f)), plotted against the y -component of each site. The ribbons are aligned such that the moiré centers (AA regions) are located at $y = 0$.

wards E_f due to the completion of the second moiré. In Fig. 5b) the local density of states (LDOS) for the blue bands in Fig. 3a)-f) is plotted against their y -component, with an explicit representation of δ , the black highlighted columns show the location around the AA centers of the moiré. As the partial moiré becomes complete, cf. red LDOS in Fig. 5b), there is a sudden localization of the electrons in the AA sites, in agreement with the experiment in Ref. [46].

The previous numerical results suggest that electronic localization plays a paramount role around E_f . To further elucidate its role, we perform a localization analysis using the inverse participation ratio (IPR), which is widely used as a measure of wavefunction localization [60–63]. It is defined as,

$$\text{IPR}(E) = \sum_i |\psi_{i,k}(E)|^4, \quad (7)$$

where the sum runs over the atomic sites. For extended states, the $\text{IPR}(E)$ scales as $1/N$, where N is the number of atoms while for localized states goes as $\text{IPR}(E) \propto 1/N^0$. A clearer description is obtained by using the

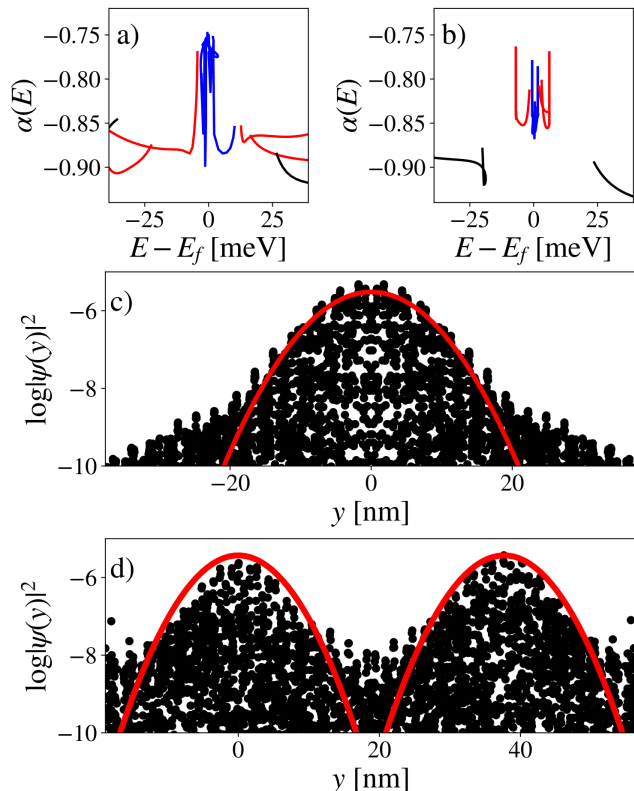


FIG. 6. Normalized inverse participation ratio $\alpha(E)$ for a) $\delta = 0$ and b) $\delta = 0.25W$, as expected the peaks occur around E_f where we have the highly localized states at the AA regions. We show in black dots the logarithm of the numerical probability densities for states near E_f against their y -coordinate for c) $\delta = 0$ and d) $\delta = 0.25W$. The red line corresponds to a Gaussian probability density in which the standard deviation is chosen to match the IPR of the corresponding state. We can see a good agreement around the localization centers.

normalized IPR, which is defined as [62],

$$\alpha(E) = \frac{\log(\text{IPR}(E))}{\log(N)}, \quad (8)$$

and thus its range is between -1 and 0. In Fig. 6, we display $\alpha(E)$ for the bands near E_f , using the same color code (blue and red) as in Fig. 3a)-f). Panels a) and b) shows $\alpha(E)$ for $\delta = 0$ (a whole moiré at the center and moiré halves at the edges) and $\delta = 0.25W$ (two complete moirés), respectively. As expected, the highest $\alpha(E)$ is located around E_f corresponding to the flat bands (indicated in blue). It is even greater for $\delta = 0$ as states are localized around just one moiré. The $\alpha(E)$ corresponding to the bands that merge with the flat bands (red bands), change their localization behavior becoming technically localized as flat bands for $\delta = 0.25W$. All these results suggest that states do have peculiar localization properties around E_f . This is further corroborated in Fig. 6c)-d), where we display the logarithm of the electron den-

sity projected along the nanoribbon cross-section. The density tracks the centers of the moiré unitary cells as expected.

Moreover, a recent analysis of TBG continuous models suggest that flat band states are akin to coherent-Landau states [64–66]. Also, flat band states in strained graphene nanoribbons have been proved to be pseudo-Landau level states akin to soliton states due to topological boundaries in the Jackiw-Rebbi model [66]. In both cases, a nearly Gaussian envelope of the flat band states was found. This has also been confirmed in calculations that allows to factorize a lowest-Landau level part in the flat-band wavefunction [67–70].

Here a nearly Gaussian-type of localization can be seen in Fig. 6c)-d) as the maximal $\log|\psi(r)|^2$ for a given y seem to be limited by downwards parabolas centered at AA sites. Thus we propose a nearly Gaussian wavefunction with a standard deviation σ such that their IPRs match, i.e., to equate the IPRs of the numerical results we use a Gaussian wavefunction with σ given by,

$$\sigma = \sqrt{\frac{1}{2\pi\text{IPR}(E)}}. \quad (9)$$

For each case we pick a state near E_f and plot $\log|\psi(r)|^2$ against its corresponding Gaussian fit, indicated by the red curves in Fig. 6c)-d) for $\delta = 0$ and $\delta = 0.25W$ respectively. The excellent matching between the red curves and the numerical results near the AA regions indicates a Gaussian behavior in such parts. However, there are clearly fat tails in Fig. 6c) when compared with a Gaussian indicating the particular shape and properties of flat band functions. These fat tails are responsible for the overlap between different AA regions and highlight the interesting nature of flat-band states. Also, the strong tendency for Gaussian localization in AA regions shown here explains why the nanoribbon width does not affect much the spectrum, instead, is the breaking of the AA regions by edges, in agreement with the experiment in Ref. [46]. The strong localization can also be used to estimate the effects of edges used a toy model based on confinement effects as will be explained in the following section.

C. Toy Model: Moiré Potential Well

As shown in Fig. 4, the lowering of the bands energy towards E_f as δ increases is composed of two effects. The first one is the global tendency associated to the confinement. This effect can be explained within the moiré quantum well picture. As confined states mainly localized in a quantum well have an energy dependence of $E(L) \propto 1/L^2$, where L is the length of the well. Thus, when we increase the parameter δ , the size of the well is increased and this lowers the energy due to less quantum confinement. We then propose that the energy of the bands localized at the partial moiré have the following δ

dependence,

$$E_{AA}(\delta) = E_0 + \frac{AW^2}{(\delta - \delta_0)^2}, \quad (10)$$

where A and E_0 are coefficients to be determined, and $\delta_0 = -0.25W$ is the value where the partial moiré cell vanishes completely. With the numerical data we can use the conditions at $E_{AA}(\delta = 0) = 0$ and $E_{AA}(\delta = 0.25W) = 88$ meV to obtain the coefficients in Eq. (10), which give $A = 7.33$ meV and $E_0 = -29.33$ meV. In Fig. 7a) we plot the curve given by Eq. (10) using these parameters alongside the numerical results. Clearly, Eq. (10) correctly describes the energy lowering without the oscillating component. As we stated in the previous section, the oscillation wavelength is invariant prior to the rescaling, and this indicates that its origin comes from the graphene lattice. One thing to notice is that due to the rotation angle, the graphene lattice is not aligned with the ribbon's periodicity, thus there is a discontinuity in the *armchair* edge at which a small *zigzag* border appears. We found that the values of δ at which the oscillation has its local maximums occur when this *zigzag* border lies in the *AB* regions, while the local minimums occur when it is in the *AA* regions. In Fig. 7b)-c) we display the bands and corresponding edges for two values of δ indicated by an square and circle in Fig. 7a), respectively. Both ribbons have moiré cells of roughly the same size.

Therefore, we recognize that the position of the *zigzag* border moves periodically as a function of δ , and its periodicity corresponds to λ , the wavelength of the small oscillation in the spectrum. Thus, we propose that the *zigzag* edges are responsible for the oscillating perturbation to the spectrum, we model them as,

$$\Delta E(\delta) = B(e^{-(\delta+\delta_0)/\gamma} - 1)\cos\left(\frac{2\pi\delta}{\lambda}\right). \quad (11)$$

Here, B is the amplitude of the perturbation, and γ modulates an exponential decay that we included to control the strength of the perturbation. As the moiré becomes mostly complete, the spectrum is predominantly governed by the moiré well. The energy of these states, mainly localized at the partial moiré, as a function of δ is then,

$$E(\delta) = E_{AA}(\delta) + \Delta E(\delta). \quad (12)$$

We found that $B = -32$ meV and $\gamma = 0.4W$ fit the numerical results as shown in Fig. 7a). Interestingly, the large scale oscillations that we found are consistent with those reported in Ref. [50]. However, it seems that the impact of the small oscillations was not been fully considered. This perturbation of the moiré flat bands has not been reported to our knowledge, and the exact form of the coupling between moiré and edge states still requires further research [43, 45]. Furthermore, in a real sample, regions with *zigzag* edges this coupling will inevitably

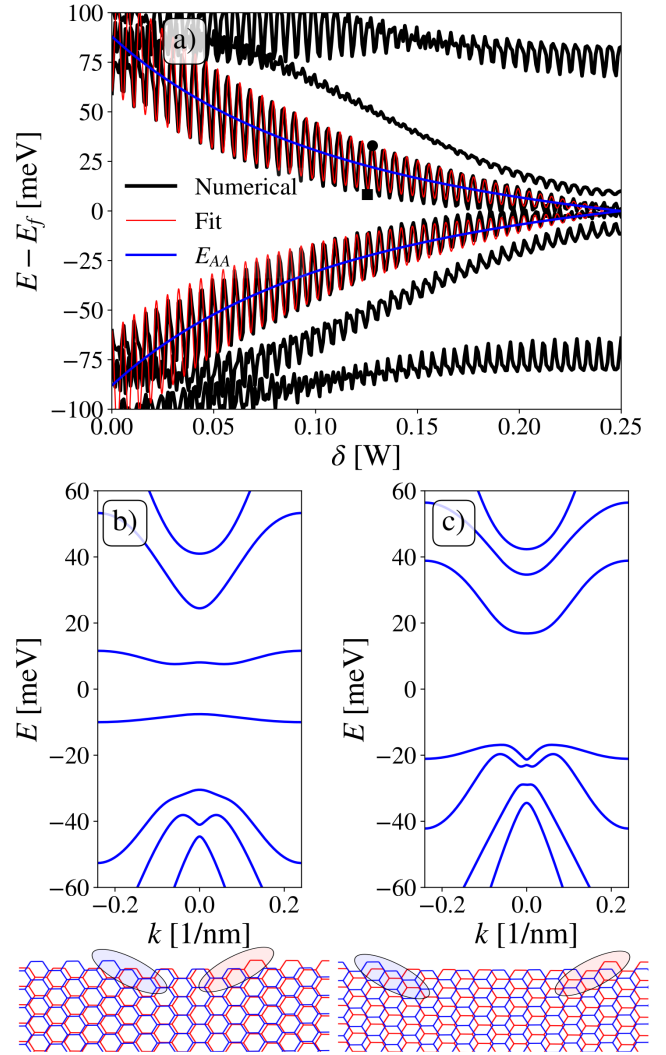


FIG. 7. a) Energy near E_f of the bands at the Brillouin zone borders for $\theta = 1.08^\circ$ and $W = 11.3$ nm (1 moiré cell). The black lines show the numerical results, while the red lines is a fit obtained by considering a change in energy akin to a quantum well as a function of the well's width (blue line), plus an oscillating perturbation originated by the *zigzag* borders. The square and circle markers shows respectively the local minimum and maximum for similar values of δ . The low-energy spectrum and the edges of the ribbon is shown for both cases indicated by the markers. In b) the bands are nearer to E_f and the *zigzag* edges are at *AA* stacking sites, while in c) the bands are further away from E_f and the *zigzag* edges are at *AB* sites.

emerge. Therefore, to complement this work, in the following section, we provide a similar analysis to the one shown in Fig. 3 but for *zigzag*-terminated nanoribbons.

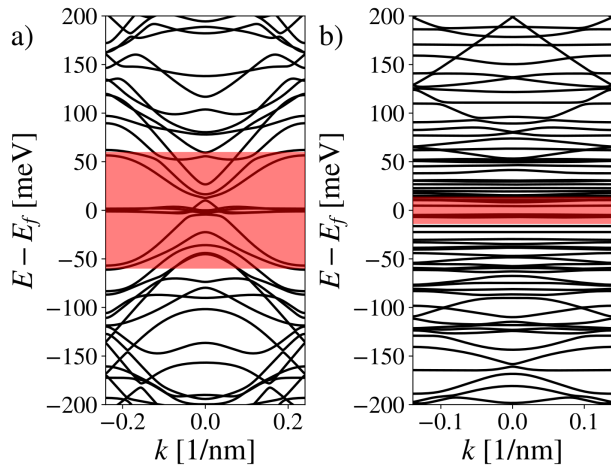


FIG. 8. Energy spectrum for TBG nanoribbons with a) *armchair* termination and a width $W_{AC} = 22.6$ nm and b) *zigzag* termination and a width $W_{ZZ} = 13$ nm. Both ribbons are considered with $\delta = 0$ such that each ribbons has a complete moiré at the center and moiré halves at the borders. The red highlighted areas in a) and b) show the energy windows at which the spectrum is shown in Fig. 3 and Figs. 9 and 10 respectively.

IV. ZIGZAG TERMINATED TBG NANORIBBONS

In this section, we investigate the scenario of *zigzag* terminated TBG nanoribbons. The ribbon's unit cell is illustrated in Fig. 1c). Unlike the *armchair* case in the previous section, the *zigzag* configuration can be achieved through a translation of a single shaded cell along the y -direction. Figure 8 depicts a comparison of the band structure for the nanoribbons of the two considered configurations. The energy bands for the *zigzag* configuration in Fig. 8b) indicate the presence of low-dispersive states even at high energies. In contrast, for the *armchair* configuration in Fig. 8a), apart from the localized states in the middle of the spectra, there are fewer low-dispersive energy states.

In the previous section, we found that the states in the small regions with *zigzag* edges, as shown in Fig. 7b)-c), are responsible for the small oscillations of the moiré bands, as seen in Fig. 7a). However, the perturbation at the moiré scale is minor and the spectrum is dominated by bulk bands, in this situation, the spectrum for the *armchair* termination clearly shows the flat-band structure of TBG. In contrast, for a *zigzag* nanoribbon, the boundaries generate several edge states that significantly impact the moiré spectrum, as depicted in Fig. 8b).

In Fig. 9 and Fig. 10, we characterize different moiré terminations by modifying the sliding parameter δ . We ensure that there is always at least one complete moiré within the ribbon. Our focus is on the energy range marked by the red shaded region in Fig. 8b). It is worth

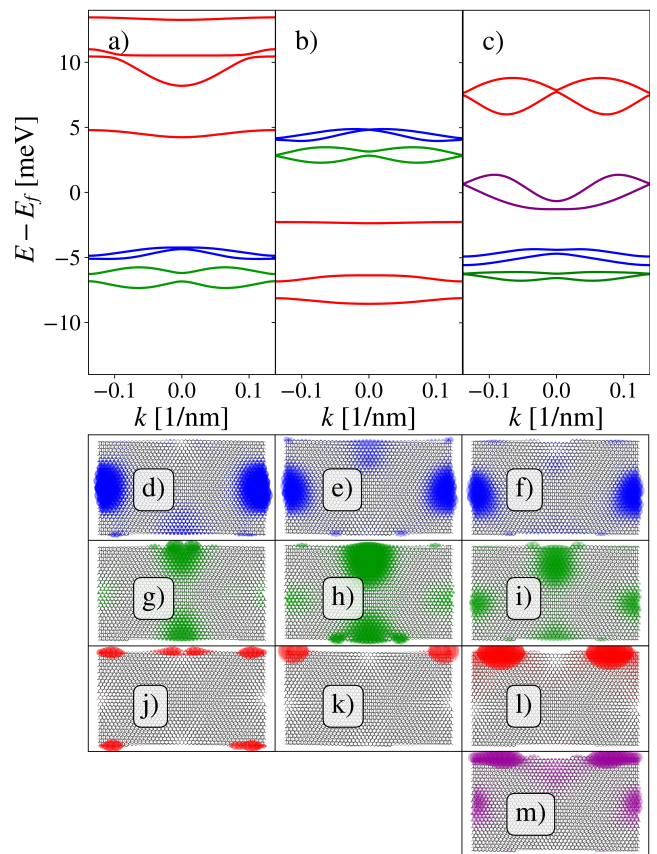


FIG. 9. Low energy band structure for *zigzag terminated* TBG nanoribbons simulating a twist angle $\theta = 1.08^\circ$ with constant width $W = 13$ nm but for different terminations obtained by translating the ribbon unit cell by a) $\delta = 0$, b) $\delta = 0.05W$ and c) $\delta = 0.1W$. We color the bands near E_f according to their localization, blue for states localized near the AA regions of the mostly complete moiré cells near the center of the ribbon, green for the states localized near the AA regions of the incomplete moiré cells near the ribbon edges, red for edge states and purple for states localized at both AA regions and edges. Below each set of bands we plot the corresponding charge density indicated with the same color code.

noting that this energy range is narrower than that of the *armchair* case due to the denser spectrum near the Fermi energy. Figures 9a)-c) and 10a)-c) depicts the band structure for different sliding values. We classify the bands according to their localization: blue for bands mostly localized at the AA regions, red for edge states, green for (mixed) states that are a mixture between AA localized and moiré edge states, and purple for those that are a mixture between AA localized and edge states. We notice the difference between moiré edge state and edge state, while the first one is an state mainly localized in an incomplete moiré along the edge (green), the second one is an state mainly localized on the zigzag sites along the boundary (red). The evolution of the states as the sliding parameter is modified is not as straightforward as

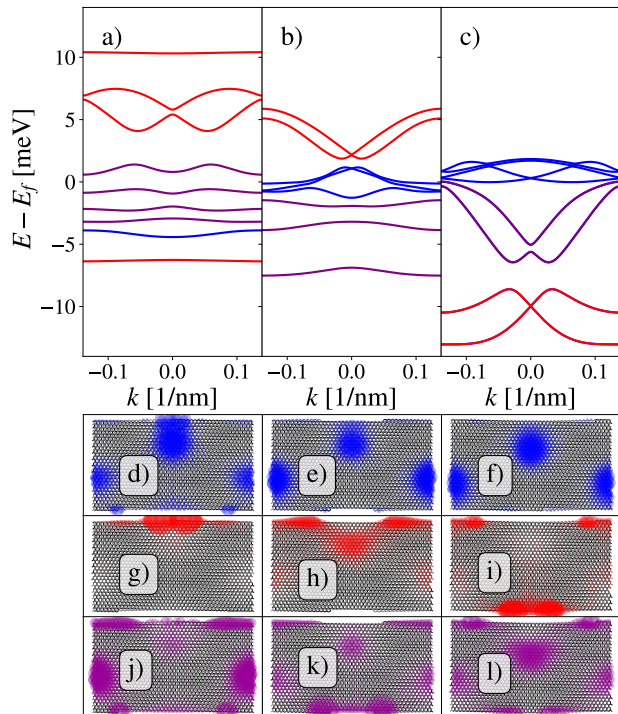


FIG. 10. Low energy band structure for *zigzag terminated* TBG nanoribbons simulating a twist angle $\theta = 1.08^\circ$ with constant width $W = 13$ nm, we consider different moiré terminations by translating the unit cell of the ribbon by a) $\delta = 0.15W$, b) $\delta = 0.2W$ and c) $\delta = 0.25W$. We color the bands near E_f according to their localization, blue for states localized near the AA regions, red for edge states and purple for states localized at both AA regions and edges. Below each set of bands we plot the total charge density in the bands of the respective color.

in the *armchair* case, as each edge and bulk state has a different energy due to the border geometry. This complexity makes it challenging to differentiate them solely based on their energy and reveals the impact of the edge microscopic boundary in the electronic spectrum.

In Fig. 9d-m) and Fig. 10d-l) we show the total charge density for the corresponding band structures. This helps us distinguish the localization of states in the different energy bands. Below each band structure we show the charge density for the bulk, edge, and mixed bands. It is important to note that this classification is not strict; we are using it solely to differentiate the states based on their maximum localization. Under this criterion, as shown in Fig. 9 and Fig. 10, is clear that the bulk moiré bands (blue), are mainly localized in the AA centers, while the edge states (red), mainly appear at the AB regions. These edge states are reminiscent of the monolayer *zigzag* configuration [51, 52] and their localization in the AB sites is in agreement with experiments in moiré structures of graphite [40, 41].

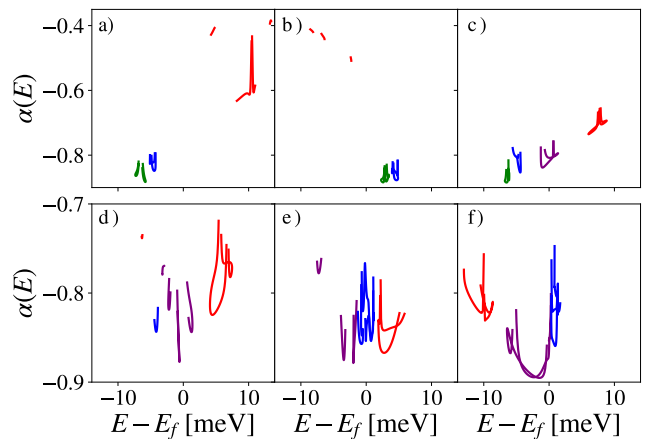


FIG. 11. Normalized inverse participation ratio $\alpha(E)$. Panels a-c) correspond to the bands shown in Fig. 9 and d-f) for the bands in Fig. 10. The color code is the same as in Fig. 9-10. As expected, the most localized states usually correspond to edge states (red) as they are distributed between a small number of atoms, especially in a) and b). Notice the different scales used between a)-c) and d)-f). On the contrary case, states that are distributed between the AA regions and the edges (purple) usually have the lowest value of $\alpha(E)$.

To characterize the different bulk and edge charge contributions, we now perform a localization analysis. Figure 11 shows the parameter $\alpha(E)$ in Eq. 8 around E_f . In the top panels, the mixed states (green) mostly occupy the incomplete moiré cells with a small contribution from the AA centers, cf. Fig 9g-i), resulting in a low value of $\alpha(E)$. The values of $\alpha(E)$ for the blue states are just slightly above the green ones, as they are mostly contained within the complete moiré cells. Both blue and green states have a similar value of their $\alpha(E)$ to those of the *armchair* case as they arise from the moiré pattern. However, the red edge states show a clear difference in magnitude as they are distributed in a smaller number of atomic sites. In the bottom panels, Fig. 11d-f), the edge states are not as localized as in the previous case, most of them are partially hybridized with moiré states (notice the difference in the scales). The purple states are highly hybridized moiré and edge states, and thus have the lowest values of $\alpha(E)$ in most cases. The blue states on the other hand, have their maximum value of $\alpha(E)$ for $\delta = 0.25W$, as this is the point where the two different moiré cells present are mostly complete, thus the wavefunction becomes maximally localized within the AA regions.

A recent experiment [46] has reported that the low energy flat band can exist as long as the moiré cell remains complete. Tunneling spectra revealed moiré AA spots when the tip was inside the sample. However, an absence of localization due to an incomplete moiré was observed at the boundary. As previously described for an armchair configuration, we have found that the nearly Gaussian localization of the moiré bulk states survives if

the moiré is complete, cf. Fig. 6c)-d) and is suppressed if the moiré is incomplete, cf. Fig. 5b). This effect is also present in a *zigzag* geometry, where the maximum localization is when the moiré is completed, cf. Fig. 11f). Interestingly, we found that if the moiré is incomplete, there is a strong hybridization with less localized edge states.

In the experiment described in Ref. [46], the edge orientation predominantly features a *zigzag* termination. Their results indicated a breakdown of the localized flat bands for an incomplete moiré, and they also reported the presence of edge states in their LDOS maps, aligning with our findings in Fig. 9. These edge states, represented by the red and green states in Fig. 9, manifest as residual LDOS peaks in incomplete moirés and rapidly decay with distance from the edges. The AA localized states only appear in complete moirés, in agreement with the blue states in Fig. 10. Given that the bulk localization is linked to the TBG flat bands, our results demonstrate their sensitivity near the boundaries. Furthermore, for ribbons with widths spanning multiple moiré cells, the flat bands in the bulk remain unperturbed as we modify the borders. We believe that our work comprehensively captures the essential characteristics of both bulk and edge states in TBG nanoribbons and it offers a detailed explanation for the experimental results in Ref. [46].

V. CONCLUSIONS

In this work, we have examined the effects of edges on the electronic properties of twisted bilayer graphene nanoribbons. Using a tight-binding model, we characterized the edge and bulk states in nanoribbons with *zigzag* and *armchair* edge terminations. We found that the flat bands in ribbons with widths spanning multiple moiré cells remain insensitive to edge modifications. However, near the boundaries, flat band localization is sensitive to the edge termination. We observed that the flat band exhibits nearly Gaussian localization, which is suppressed if the moiré is incomplete. Additionally, depending on the edge orientation, bulk states can hybridize with the edge states.

In *armchair*-terminated nanoribbons, the low-energy

spectrum is determined by the completeness of the moiré cells at the ribbon's edge, transitioning from dispersive to flat bands as the moiré cell becomes complete. This behavior aligns with a moiré quantum well picture. There is also a perturbation in the band's energy due to the appearance of small regions with *zigzag* termination. Depending on whether these *zigzag* borders appear on AA or AB stacking regions, the band energy is either lowered or raised, while the main Gaussian-like localization in the AA regions remains. These *zigzag* regions will inevitably appear due to the mismatch between the ribbon alignment and the armchair direction.

In *zigzag*-terminated nanoribbons, there is a more pronounced impact on the low-energy spectrum due to the edge states, as they can become hybridized with the moiré states. However, some states remain predominantly localized within the AA regions. The influence of the edge states is expected to be diminished in real samples as translational symmetry is reduced, resulting in a mixture of armchair and *zigzag* boundaries. As in the *armchair* case, the behavior should primarily be described by the bands localized within the AA regions. Consequently, regardless of the edge termination, we expect AA localization when the moiré is complete and delocalization when it is not. Our findings provide an explanation for the breakdown of flat bands and the co-existence of bulk and edge states in recent experiments with twisted bilayer graphene nanoribbons [46]

VI. ACKNOWLEDGMENTS

We thank Héctor Sainz-Cruz for fruitful discussions. This work was supported by UNAM DGAPA PAPIIT IN102620 (E.A. and G.G.N.), CONAHCyT project 1564464 (E.A.,G.G.N.). IMDEA Nanociencia acknowledges support from the “Severo Ochoa” Programme for Centres of Excellence in R&D (Grant No. SEV-2016-0686). P.A.P and F.G. acknowledge funding from the European Commission, within the Graphene Flagship, Core 3, grant number 881603 and from grants NMAT2D (Comunidad de Madrid, Spain), SprQuMat and (MAD2D-CM)-MRR MATERIALES AVANZADOS-IMDEA-NC.

-
- [1] Yuan Cao, Valla Fatemi, Shiang Fang, Kenji Watanabe, Takashi Taniguchi, Efthimios Kaxiras, and Pablo Jarillo-Herrero. Unconventional superconductivity in magic-angle graphene superlattices. *Nature*, 556(7699):43–50, 2018.
- [2] Matthew Yankowitz, Shaowen Chen, Hryhorii Polshyn, Yuxuan Zhang, K Watanabe, T Taniguchi, David Graf, Andrea F Young, and Cory R Dean. Tuning superconductivity in twisted bilayer graphene. *Science*, 363(6431):1059–1064, 2019.
- [3] Yuan Cao, Valla Fatemi, Ahmet Demir, Shiang Fang, Spencer L Tomarken, Jason Y Luo, Javier D Sanchez-Yamagishi, Kenji Watanabe, Takashi Taniguchi, Efthimios Kaxiras, et al. Correlated insulator behaviour at half-filling in magic-angle graphene superlattices. *Nature*, 556(7699):80–84, 2018.
- [4] Kevin P Nuckolls, Myungchul Oh, Dillon Wong, Biao Lian, Kenji Watanabe, Takashi Taniguchi, B Andrei Bernevig, and Ali Yazdani. Strongly correlated chern insulators in magic-angle twisted bilayer graphene. *Nature*, 588(7839):610–615, 2020.

- [5] Andrew T Pierce, Yonglong Xie, Jeong Min Park, Eslam Khalaf, Seung Hwan Lee, Yuan Cao, Daniel E Parker, Patrick R Forrester, Shaowen Chen, Kenji Watanabe, et al. Unconventional sequence of correlated chern insulators in magic-angle twisted bilayer graphene. *Nature Physics*, 17(11):1210–1215, 2021.
- [6] Aaron L. Sharpe, Eli J. Fox, Arthur W. Barnard, Joe Finney, Kenji Watanabe, Takashi Taniguchi, M. A. Kastner, and David Goldhaber-Gordon. Emergent ferromagnetism near three-quarters filling in twisted bilayer graphene. *Science*, 365(6453):605–608, August 2019.
- [7] Xiaobo Lu, Petr Stepanov, Wei Yang, Ming Xie, Mohammed Ali Aamir, Ipsita Das, Carles Urgell, Kenji Watanabe, Takashi Taniguchi, Guangyu Zhang, et al. Superconductors, orbital magnets and correlated states in magic-angle bilayer graphene. *Nature*, 574(7780):653–657, 2019.
- [8] Hryhoriy Polshyn, Matthew Yankowitz, Shaowen Chen, Yuxuan Zhang, K. Watanabe, T. Taniguchi, Cory R. Dean, and Andrea F. Young. Large linear-in-temperature resistivity in twisted bilayer graphene. *Nature Physics*, 15(10):1011–1016, August 2019.
- [9] M. Serlin, C. L. Tschirhart, H. Polshyn, Y. Zhang, J. Zhu, K. Watanabe, T. Taniguchi, L. Balents, and A. F. Young. Intrinsic quantized anomalous hall effect in a moiré heterostructure. *Science*, 367(6480):900–903, February 2020.
- [10] Guorui Chen, Aaron L. Sharpe, Eli J. Fox, Ya-Hui Zhang, Shaoxin Wang, Lili Jiang, Bosai Lyu, Hongyuan Li, Kenji Watanabe, Takashi Taniguchi, Zhiwen Shi, T. Senthil, David Goldhaber-Gordon, Yuanbo Zhang, and Feng Wang. Tunable correlated chern insulator and ferromagnetism in a moiré superlattice. *Nature*, 579(7797):56–61, March 2020.
- [11] Yu Saito, Jingyuan Ge, Kenji Watanabe, Takashi Taniguchi, and Andrea F. Young. Independent superconductors and correlated insulators in twisted bilayer graphene. *Nature Physics*, 16(9):926–930, June 2020.
- [12] U. Zondiner, A. Rozen, D. Rodan-Legrain, Y. Cao, R. Queiroz, T. Taniguchi, K. Watanabe, Y. Oreg, F. von Oppen, Ady Stern, E. Berg, P. Jarillo-Herrero, and S. Ilani. Cascade of phase transitions and dirac revivals in magic-angle graphene. *Nature*, 582(7811):203–208, June 2020.
- [13] Dillon Wong, Kevin P. Nuckolls, Myungchul Oh, Biao Lian, Yonglong Xie, Sangjun Jeon, Kenji Watanabe, Takashi Taniguchi, B. Andrei Bernevig, and Ali Yazdani. Cascade of electronic transitions in magic-angle twisted bilayer graphene. *Nature*, 582(7811):198–202, June 2020.
- [14] Petr Stepanov, Ipsita Das, Xiaobo Lu, Ali Fahimniya, Kenji Watanabe, Takashi Taniguchi, Frank H. L. Koppens, Johannes Lischner, Leonid Levitov, and Dmitri K. Efetov. Untying the insulating and superconducting orders in magic-angle graphene. *Nature*, 583(7816):375–378, July 2020.
- [15] Yang Xu, Song Liu, Daniel A. Rhodes, Kenji Watanabe, Takashi Taniguchi, James Hone, Veit Elser, Kin Fai Mak, and Jie Shan. Correlated insulating states at fractional fillings of moiré superlattices. *Nature*, 587(7833):214–218, November 2020.
- [16] Youngjoon Choi, Hyunjin Kim, Yang Peng, Alex Thomson, Cyprian Lewandowski, Robert Polski, Yiran Zhang, Harpreet Singh Arora, Kenji Watanabe, Takashi Taniguchi, Jason Alicea, and Stevan Nadj-Perge. Correlation-driven topological phases in magic-angle twisted bilayer graphene. *Nature*, 589(7843):536–541, January 2021.
- [17] Asaf Rozen, Jeong Min Park, Uri Zondiner, Yuan Cao, Daniel Rodan-Legrain, Takashi Taniguchi, Kenji Watanabe, Yuval Oreg, Ady Stern, Erez Berg, Pablo Jarillo-Herrero, and Shahal Ilani. Entropic evidence for a pomeranchuk effect in magic-angle graphene. *Nature*, 592(7853):214–219, April 2021.
- [18] Yuan Cao, Daniel Rodan-Legrain, Jeong Min Park, Noah F. Q. Yuan, Kenji Watanabe, Takashi Taniguchi, Rafael M. Fernandes, Liang Fu, and Pablo Jarillo-Herrero. Nematicity and competing orders in superconducting magic-angle graphene. *Science*, 372(6539):264–271, April 2021.
- [19] Petr Stepanov, Ming Xie, Takashi Taniguchi, Kenji Watanabe, Xiaobo Lu, Allan H. MacDonald, B. Andrei Bernevig, and Dmitri K. Efetov. Competing zero-field chern insulators in superconducting twisted bilayer graphene. *Phys. Rev. Lett.*, 127:197701, Nov 2021.
- [20] Myungchul Oh, Kevin P. Nuckolls, Dillon Wong, Ryan L. Lee, Xiaomeng Liu, Kenji Watanabe, Takashi Taniguchi, and Ali Yazdani. Evidence for unconventional superconductivity in twisted bilayer graphene. *Nature*, 600(7888):240–245, October 2021.
- [21] Yonglong Xie, Andrew T. Pierce, Jeong Min Park, Daniel E. Parker, Eslam Khalaf, Patrick Ledwith, Yuan Cao, Seung Hwan Lee, Shaowen Chen, Patrick R. Forrester, Kenji Watanabe, Takashi Taniguchi, Ashvin Vishwanath, Pablo Jarillo-Herrero, and Amir Yacoby. Fractional chern insulators in magic-angle twisted bilayer graphene. *Nature*, 600(7889):439–443, December 2021.
- [22] Alexey I. Berdyugin, Na Xin, Haoyang Gao, Sergey Slizovskiy, Zhiyu Dong, Shubhadeep Bhattacharjee, P. Kumaravadivel, Shuigang Xu, L. A. Ponomarenko, Matthew Holwill, D. A. Bandurin, Minsoo Kim, Yang Cao, M. T. Greenaway, K. S. Novoselov, I. V. Grigorieva, K. Watanabe, T. Taniguchi, V. I. Fal’ko, L. S. Levitov, Roshan Krishna Kumar, and A. K. Geim. Out-of-equilibrium criticalities in graphene superlattices. *Science*, 375(6579):430–433, January 2022.
- [23] Simon Turkel, Joshua Swann, Ziyang Zhu, Maine Christos, K. Watanabe, T. Taniguchi, Subir Sachdev, Mathias S. Scheurer, Efthimios Kaxiras, Cory R. Dean, and Abhay N. Pasupathy. Orderly disorder in magic-angle twisted trilayer graphene. *Science*, 376(6589):193–199, April 2022.
- [24] Tianye Huang, Xuecou Tu, Changqing Shen, Binjie Zheng, Junzhan Wang, Hao Wang, Kaveh Khaliji, Sang Hyun Park, Zhiyong Liu, Teng Yang, Zhidong Zhang, Lei Shao, Xuesong Li, Tony Low, Yi Shi, and Xiaomu Wang. Observation of chiral and slow plasmons in twisted bilayer graphene. *Nature*, 605(7908):63–68, May 2022.
- [25] P. San-Jose, J. González, and F. Guinea. Non-abelian gauge potentials in graphene bilayers. *Phys. Rev. Lett.*, 108:216802, May 2012.
- [26] J. M. B. Lopes dos Santos, N. M. R. Peres, and A. H. Castro Neto. Continuum model of the twisted graphene bilayer. *Phys. Rev. B*, 86:155449, Oct 2012.
- [27] G. Trambly de Laissardière, D. Mayou, and L. Magaud. Numerical studies of confined states in rotated bilayers of graphene. *Phys. Rev. B*, 86:125413, Sep 2012.
- [28] A. Luican, Guohong Li, A. Reina, J. Kong, R. R. Nair, K. S. Novoselov, A. K. Geim, and E. Y. Andrei. Single-

- layer behavior and its breakdown in twisted graphene layers. *Phys. Rev. Lett.*, 106:126802, Mar 2011.
- [29] Long-Jing Yin, Jia-Bin Qiao, Wei-Jie Zuo, Wen-Tian Li, and Lin He. Experimental evidence for non-abelian gauge potentials in twisted graphene bilayers. *Phys. Rev. B*, 92:081406, Aug 2015.
- [30] Yonglong Xie, Biao Lian, Berthold Jäck, Xiaomeng Liu, Cheng-Li Chiu, Kenji Watanabe, Takashi Taniguchi, B Andrei Bernevig, and Ali Yazdani. Spectroscopic signatures of many-body correlations in magic-angle twisted bilayer graphene. *Nature*, 572(7767):101–105, 2019.
- [31] Yuhang Jiang, Xinyuan Lai, Kenji Watanabe, Takashi Taniguchi, Kristjan Haule, Jinhai Mao, and Eva Y Andrei. Charge order and broken rotational symmetry in magic-angle twisted bilayer graphene. *Nature*, 573(7772):91–95, 2019.
- [32] Youngjoon Choi, Hyunjin Kim, Yang Peng, Alex Thomson, Cyprian Lewandowski, Robert Polski, Yiran Zhang, Harpreet Singh Arora, Kenji Watanabe, Takashi Taniguchi, et al. Correlation-driven topological phases in magic-angle twisted bilayer graphene. *Nature*, 589(7843):536–541, 2021.
- [33] J. M. B. Lopes dos Santos, N. M. R. Peres, and A. H. Castro Neto. Graphene bilayer with a twist: Electronic structure. *Phys. Rev. Lett.*, 99:256802, Dec 2007.
- [34] S. Shallcross, S. Sharma, and O. A. Pankratov. Quantum interference at the twist boundary in graphene. *Phys. Rev. Lett.*, 101:056803, Aug 2008.
- [35] S. Shallcross, S. Sharma, E. Kandelaki, and O. A. Pankratov. Electronic structure of turbostratic graphene. *Phys. Rev. B*, 81:165105, Apr 2010.
- [36] Rafi Bistritzer and Allan H. MacDonald. Moiré bands in twisted double-layer graphene. *Proceedings of the National Academy of Sciences*, 108(30):12233–12237, July 2011.
- [37] G. Trambly de Laissardière, D. Mayou, and L. Magaud. Localization of dirac electrons in rotated graphene bilayers. *Nano Letters*, 10(3):804–808, February 2010.
- [38] E. J. Mele. Commensuration and interlayer coherence in twisted bilayer graphene. *Phys. Rev. B*, 81:161405(R), Apr 2010.
- [39] W. Landgraf, S. Shallcross, K. Türschmann, D. Weckbecker, and O. Pankratov. Electronic structure of twisted graphene flakes. *Phys. Rev. B*, 87:075433, Feb 2013.
- [40] E. Suárez Morell, R. Vergara, M. Pacheco, L. Brey, and Leonor Chico. Electronic properties of twisted bilayer nanoribbons. *Phys. Rev. B*, 89:205405, May 2014.
- [41] E. Suárez Morell, P. Vargas, P. Häberle, Samuel A. Hevia, and Leonor Chico. Edge states of moiré structures in graphite. *Phys. Rev. B*, 91:035441, Jan 2015.
- [42] Huaihua Shao and Guanghui Zhou. Local atomic-morphology-resolved edge states in twisted bilayer graphene nanoribbons. *Journal of Physics: Condensed Matter*, 35(3):035301, November 2022.
- [43] M Fleischmann, R Gupta, D Weckbecker, W Landgraf, O Pankratov, V Meded, and S Shallcross. Moiré edge states in twisted graphene nanoribbons. *Physical Review B*, 97(20):205128, 2018.
- [44] Matthieu Fortin-Deschênes, Rui Pu, Yan-Feng Zhou, Chao Ma, Patrick Cheung, Kenji Watanabe, Takashi Taniguchi, Fan Zhang, Xu Du, and Fengnian Xia. Uncovering topological edge states in twisted bilayer graphene. *Nano Letters*, 22(15):6186–6193, July 2022.
- [45] Dongfei Wang, De-Liang Bao, Qi Zheng, Chang-Tian Wang, Shiyong Wang, Peng Fan, Shantanu Mishra, Lei Tao, Yao Xiao, Li Huang, Xinliang Feng, Klaus Müllen, Yu-Yang Zhang, Roman Fasel, Pascal Ruffieux, Shixuan Du, and Hong-Jun Gao. Twisted bilayer zigzag-graphene nanoribbon junctions with tunable edge states. *Nature Communications*, 14(1), February 2023.
- [46] Long-Jing Yin, Ling-Hui Tong, Yue-Ying Zhou, Yang Zhang, Yuan Tian, Li Zhang, Lijie Zhang, and Zhihui Qin. Direct observation of moiré flat-band breakdown at the edge of magic-angle twisted bilayer graphene. *Physical Review B*, 105(20):L201405, 2022.
- [47] Ying Su and Shi-Zeng Lin. Topological sliding moiré heterostructure. *Phys. Rev. B*, 101:041113, Jan 2020.
- [48] Yinhan Zhang, Yang Gao, and Di Xiao. Topological charge pumping in twisted bilayer graphene. *Phys. Rev. B*, 101:041410, Jan 2020.
- [49] Manato Fujimoto, Henri Koschke, and Mikito Koshino. Topological charge pumping by a sliding moiré pattern. *Phys. Rev. B*, 101:041112, Jan 2020.
- [50] Manato Fujimoto and Mikito Koshino. Moiré edge states in twisted bilayer graphene and their topological relation to quantum pumping. *Phys. Rev. B*, 103:155410, Apr 2021.
- [51] Mitsutaka Fujita, Katsunori Wakabayashi, Kyoko Nakada, and Koichi Kusakabe. Peculiar localized state at zigzag graphite edge. *Journal of the Physical Society of Japan*, 65(7):1920–1923, July 1996.
- [52] Kyoko Nakada, Mitsutaka Fujita, Gene Dresselhaus, and Mildred S. Dresselhaus. Edge state in graphene ribbons: Nanometer size effect and edge shape dependence. *Phys. Rev. B*, 54:17954–17961, Dec 1996.
- [53] Xianqing Lin and David Tománek. Minimum model for the electronic structure of twisted bilayer graphene and related structures. *Physical Review B*, 98(8):081410, 2018.
- [54] J. M. B. Lopes dos Santos, N. M. R. Peres, and A. H. Castro Neto. Graphene bilayer with a twist: Electronic structure. *Phys. Rev. Lett.*, 99:256802, Dec 2007.
- [55] J. M. B. Lopes dos Santos, N. M. R. Peres, and A. H. Castro Neto. Continuum model of the twisted graphene bilayer. *Phys. Rev. B*, 86:155449, Oct 2012.
- [56] Luis A. Gonzalez-Arraga, J. L. Lado, Francisco Guinea, and Pablo San-Jose. Electrically controllable magnetism in twisted bilayer graphene. *Phys. Rev. Lett.*, 119:107201, Sep 2017.
- [57] Javad Vahedi, Robert Peters, Ahmed Missaoui, Andreas Honecker, and Guy Trambly de Laissardière. Magnetism of magic-angle twisted bilayer graphene. *SciPost Phys.*, 11:083, 2021.
- [58] Héctor Sainz-Cruz, Tommaso Cea, Pierre A. Pantaleón, and Francisco Guinea. High transmission in twisted bilayer graphene with angle disorder. *Phys. Rev. B*, 104:075144, Aug 2021.
- [59] Rafi Bistritzer and Allan H MacDonald. Moiré bands in twisted double-layer graphene. *Proceedings of the National Academy of Sciences*, 108(30):12233–12237, 2011.
- [60] RJ Bell and Paul Dean. Atomic vibrations in vitreous silica. *Discussions of the Faraday society*, 50:55–61, 1970.
- [61] JT Edwards and DJ Thouless. Numerical studies of localization in disordered systems. *Journal of Physics C: Solid State Physics*, 5(8):807, 1972.
- [62] Gerardo G. Naumis. Internal mobility edge in doped graphene: Frustration in a renormalized lattice. *Phys.*

- Rev. B*, 76:153403, Oct 2007.
- [63] Pragma Shukla. Disorder perturbed flat bands: Level density and inverse participation ratio. *Phys. Rev. B*, 98:054206, Aug 2018.
- [64] Leonardo A. Navarro-Labastida and Gerardo G. Naumis. 3/2 magic angle quantization rule of flat bands in twisted bilayer graphene and its relationship to the quantum hall effect. *Phys. Rev. B*, 107:155428, Apr 2023.
- [65] Leonardo Antonio Navarro Labastida and G. G. Naumis. Flat bands, quantum hall effect and superconductivity in twisted bilayer graphene at magic angles. *Revista Mexicana de Física*, 69(4 Jul-Aug):041602 1–, Jul. 2023.
- [66] Elias Andrade, Florentino López-Urías, and Gerardo G. Naumis. Topological origin of flat bands as pseudo-landau levels in uniaxial strained graphene nanoribbons and induced magnetic ordering due to electron-electron interactions. *Phys. Rev. B*, 107:235143, Jun 2023.
- [67] Grigory Tarnopolsky, Alex Jura Kruchkov, and Ashvin Vishwanath. Origin of magic angles in twisted bilayer graphene. *Phys. Rev. Lett.*, 122:106405, Mar 2019.
- [68] Fedor K. Popov and Alexey Milekhin. Hidden wave function of twisted bilayer graphene: Flat band as a landau level. *arXiv e-prints*, page arXiv:2010.02915, Oct 2020.
- [69] Jie Wang, Yunqin Zheng, Andrew J. Millis, and Jennifer Cano. Chiral approximation to twisted bilayer graphene: Exact intravalley inversion symmetry, nodal structure, and implications for higher magic angles. *Phys. Rev. Res.*, 3:023155, May 2021.
- [70] Yarden Sheffer and Ady Stern. Chiral magic-angle twisted bilayer graphene in a magnetic field: Landau level correspondence, exact wave functions, and fractional chern insulators. *Phys. Rev. B*, 104:L121405, Sep 2021.